Research Square

Preprints are preliminary reports that have not undergone peer review.
They should not be considered conclusive, used to inform clinical practice,
or referenced by the media as validated information.

Bypassing reductive dimerization of bottleneck PFAS intermediates via asymmetric advanced oxidation for absolute defluorination

Wenjun Sun

wsun@tsinghua.edu.cn

School of Environment, Tsinghua University

Yanei Xue

Tsinghua University

Guoqing Jiang

Tsinghua University, Chongqing University

Bing Zhang

Chongqing University https://orcid.org/0000-0003-4002-6005

Wenxin Shi

Key Laboratory of Eco-environments in Three Gorges Reservoir Region, Ministry of Education, College of Environment and Ecology, Chongqing University

Madjid Mohseni Madjid Mohseni

Chongqing University

Ted Mao

Tsinghua University

Article

Keywords:

Posted Date: September 18th, 2026

DOI: https://doi.org/10.21203/rs.3.rs-10968317/v1

License: This work is licensed under a Creative Commons Attribution 4.0 International License.
Read Full License

Additional Declarations: There is **NO** Competing Interest.

Bypassing reductive dimerization of bottleneck PFAS intermediates via asymmetric advanced oxidation for absolute defluorination

Yanei Xue[a], Wenjun Sun[a,#], Ted Mao[a], Guoqing Jiang[b], Bing Zhang[b], Wenxin Shi[b], Madjid Mohseni[c],

[a] School of Environment
Tsinghua University
Beijing, 100084, China
E-mail: wsun@tsinghua.edu.cn

[b] College of Environment and Ecology
Chongqing University
Chongqing, 400044, China

[c] Department of Chemical and Biological Engineering
University of British Columbia
2360 East Mall, Vancouver
BC Canada V6T 1Z3

Abstract:
Hydrated electron (e_{aq}^-)-based advanced reduction processes (ARPs) have been widely employed to initiate non-thermal cleavage of highly stable C—F bonds in per- and polyfluoroalkyl substances (PFAS). However, complete defluorination is rarely achieved, as downstream transformation pathways consistently stall at short-chain intermediates. In this study, the origin of this reductive arrest is elucidated. A pronounced collapse of localized electron affinity in ultra-short C2 terminal intermediates suppresses further electron injection, thereby diverting perfluorinated radicals toward self-recombination pathways that produce dimeric end products. Under vacuum ultraviolet irradiation, a coupled oxidation/reduction environment was shown to overcome this energetic limitation through an asymmetric oxidative interception pathway. Wavefunction analysis combined with Marcus-theory-based density functional theory calculations indicates that this process is governed by a highly localized orbital polarization centered on the desorbed carbon atoms of C2 intermediates. Such polarization enables near barrier-free cross-coupling with coexisting HO•, facilitating rapid capture of transient radicals before dimer formation or volatilization. This oxidative pathway redirects bottleneck intermediates toward unstable fluorinated alcohol analogues, which subsequently undergo spontaneous intramolecular ketonization, resulting in progressive fluorine elimination. To unlock chemical descriptors governing complete PFAS defluorination, a data-enhanced generative framework (VAE-ANN) was applied to more than 90 congeners. A key synergy descriptor ($\eta_{G/F}$) was thereby established to define the optimal oxidant-to-reductant ratio required for achieving complete defluorination. This work demonstrates that complete PFAS mineralization should transcend conventional metrics, such as carbon chain length, by prioritizing the mechanistic alignment between intrinsic molecular features and extrinsic reaction conditions.

Per- and polyfluoroalkyl substances (PFAS) constitute a class of highly persistent anthropogenic contaminants, necessitating a transition from phase-transfer remediation approaches to destructive mineralization strategies[1, 2]. Among available technologies, advanced reduction processes (ARPs) employing hydrated electrons (e_{aq}^-, E^0=−2.87 V vs. SHE)[3] have demonstrated strong potential for initiating parent compound degradation utilizing excitation sources such as UV/sulfite[4, 5], UV/alcohol[6], and vacuum ultraviolet (VUV)[7], with reported degradation rate constants (k_{deC}) spanning from 0.0032 h^{-1} to 17.0 h^{-1} . Despite this capability, a substantial gap remains between initial molecular breakdown and deep defluorination. While cleavage of functional headgroups or peripheral moieties is commonly observed, the quantum chemical limitations and kinetic constraints governing downstream defluorination remain poorly resolved. As a result, apparent degradation efficiency often masks incomplete fluorine removal, leaving the thermodynamic and kinetic basis of full mineralization insufficiently understood.

The limitation in deep defluorination arises from a complex interplay between molecular structure and radical reaction pathways, which cannot be adequately described by conventional thermodynamic metrics such as bond dissociation energies (BDEs)[8]. Progressive shortening of perfluorocarbon chains leads to a marked decline in localized electron affinity, particularly at ultra-short terminal fragments such as C2 intermediates. At this stage, the single-molecule electron transfer (ET) process becomes energetically unfavorable, with activation free energies ($\Delta G_{ET}^{\ddagger}$) reaching 23.3—27.4 kcal mol^{-1}[9], thereby hindering further reductive transformation. Under purely reductive conditions, these intermediates are instead redirected into kinetically favorable but unproductive pathways. For example, they may undergo recombination to form stable closed-shell dimeric species, including perfluorodicarboxylate dimers(—$O_2C(CF_2)_2CO_2$—)[10] or sulfonate-based assemblies, which contribute to persistent chemical bottlenecks. Alternatively, in proton-rich environments, hydrogen abstraction can occur, producing volatile organic fluorides (VOFs) such as CH_3CF_3, which may escape into the atmosphere or further impede

defluorination due to the strengthening of adjacent C—F bonds beyond 120 kcal mol^{-1} following H/F exchange[7, 11]. To overcome these limitations, recent approaches have explored integrated redox systems, including sequential oxidation-reduction schemes and combined UV/S-EO platforms[12], enabling near-complete defluorination through alternating chain cleavage and mineralization steps. Nevertheless, a unified mechanistic framework capable of synchronizing radical generation with efficient interception of transient intermediates remains lacking, and the kinetic basis of such coordinated processes has yet to be fully clarified.

To systematically dismantle this kinetic deadlock, the synchronous evolution of thermodynamic and kinetic descriptors across the full degradation cascade was mapped. Structural dependencies and mechanistic pathways of PFAS mineralization were investigated under a tailored VUV-driven advanced oxidation/reduction process (AO/RP). Non-targeted high-resolution mass spectrometry combined with transient high-resolution TOF-MS enabled the capture of short-lived dimeric intermediates, which were identified as the primary bottleneck limiting deep defluorination under oxidant-depleted conditions. Wavefunction analysis and density functional theory (DFT) calculations within the Marcus framework elucidated the radical interception network, demonstrating that a localized VUV-induced synergistic system overcomes the electron-transfer ceiling via asymmetric oxidative interception, achieving a near barrierless C2 radical-oxidative radical cross-coupling ($\Delta G^{\ddagger}_{\mathrm{oxidation}} \approx 0$ kcal mol^{-1}). Furthermore, a data-augmented generative framework applied to more than 90 congeners enabled the definition of a structural synergy index ($\eta_{G/F}$), which quantitatively maps the macroscopic kinetic network. This integrated molecular-to-macroscopic framework provides a predictive and precision-oriented approach for complete defluorination without bypass accumulation, thereby advancing sustainable remediation strategies and fluorochemical design.

Structural Dependency and Kinetic Divergence of PFAS under VUV Irradiation

To elucidate structural dependence and mechanistic pathways during PFAS degradation, spatial reaction zones and corresponding kinetic regimes under VUV irradiation were systematically analyzed. The fluorine mass balance exhibited strong dependence on VUV penetration depth, resulting in two distinct regimes. In the near-surface region dominated by direct photoionization (The penetration depth < 12 mm) [13, 14], the overall defluorination reached 54%, accompanied by the formation of 31% VOF (Fig. 1a). In contrast, radical-mediated redox reactions in the bulk phase achieved 98% DeF% with only 6% VOF remaining (Fig. 1d). For the direct photoionization pathway, the defluorination rate constant showed a linear correlation ($R^2 = 0.7154$) with the weakest bond dissociation energy (BDE, the specific data show in Supplementary Table 1) of target molecules, indicating that initial bond cleavage is governed by local thermodynamic stability. The correlation between defluorination rate (ln k_F) and degradation rate (ln k_G) (Fig. 1e) further revealed kinetic divergence across PFAS structures, highlighting the accumulation of structurally distinct intermediates. The ratio was distributed around the theoretical baseline, where a value of 1.0 corresponds to instantaneous mineralization without intermediate accumulation. Long-chain perfluorocarboxylic acids (PFCAs), including PFOA and PFNA, exhibited ratios between 0.82 and 0.91, indicating moderate bottleneck effects associated with stepwise chain shortening. In contrast, branched and ether-PFAS structures showed ratios exceeding 1.05, suggesting accelerated downstream fluorine release following initial structural cleavage. Perfluorinated sulfonates (PFSAs) and LiTFSI displayed pronounced plateaus below the baseline, reflecting severe kinetic limitations induced by sulfonate functionalities.

The structure-dependent accumulation of intermediates was further rationalized through quantum chemical energy profiles derived from Marcus theory (Fig. 1f). The synchronization of defluorination

cascades is governed by the interplay between thermodynamic driving force (ΔG) and reorganization energy (λ), which together determine the activation free energy barrier ($\Delta G^{\ddagger}$) for electron transfer[9, 15]. For molecular classes positioned near or above the baseline, reduced $\Delta G^{\ddagger}$ values and a relatively uniform energy landscape prevent the formation of deep energetic wells, enabling continuous defluorination. Conversely, recalcitrant structures such as PFSAs exhibit elevated $\Delta G^{\ddagger}$ values during intermediate steps, resulting in severe kinetic bottlenecks. This mismatch between thermodynamic favorability and kinetic accessibility slows intermediate transformation relative to parent degradation, producing macroscopic stagnation and pronounced deviations in defluorination-degradation relationships.

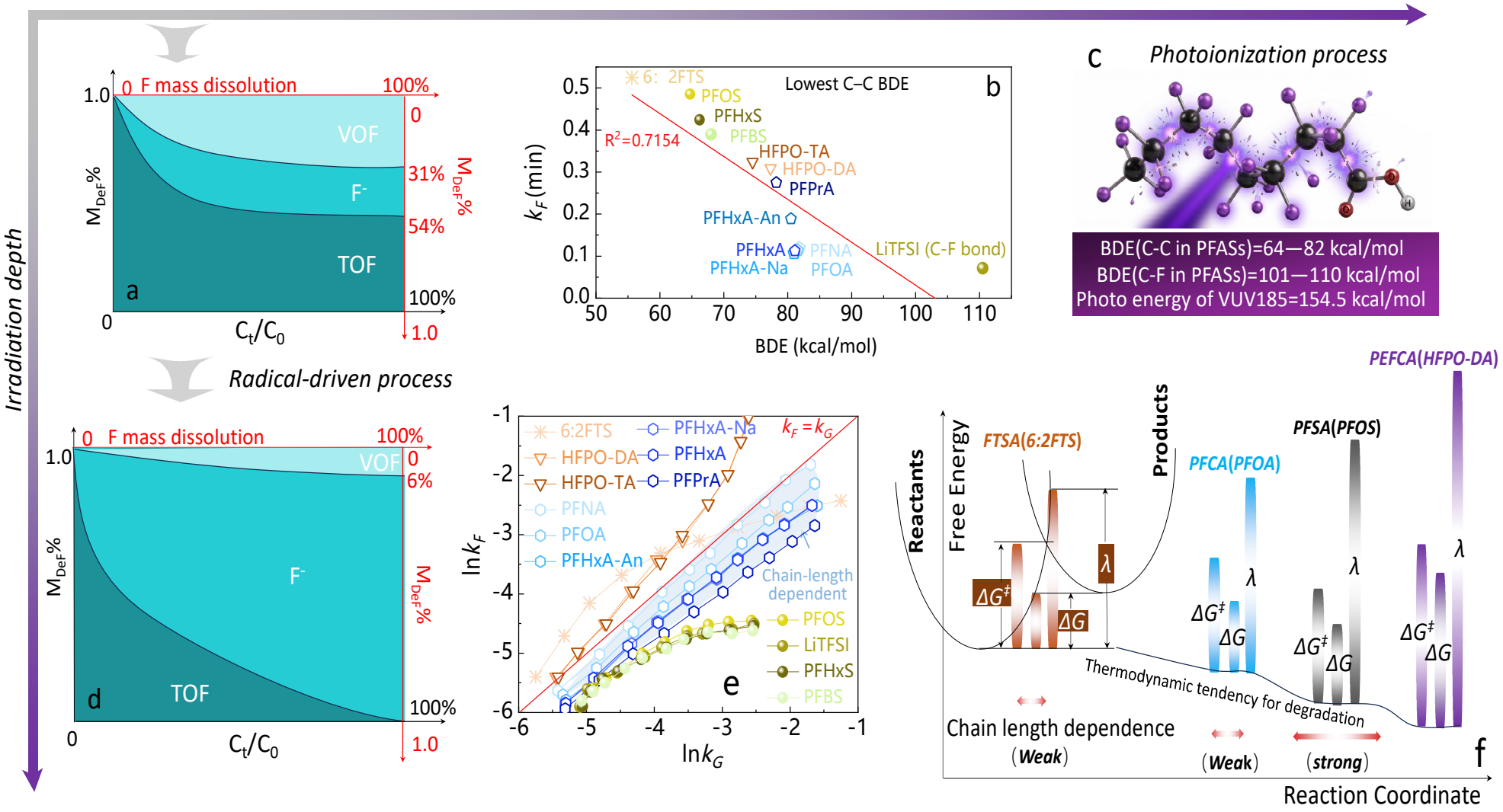


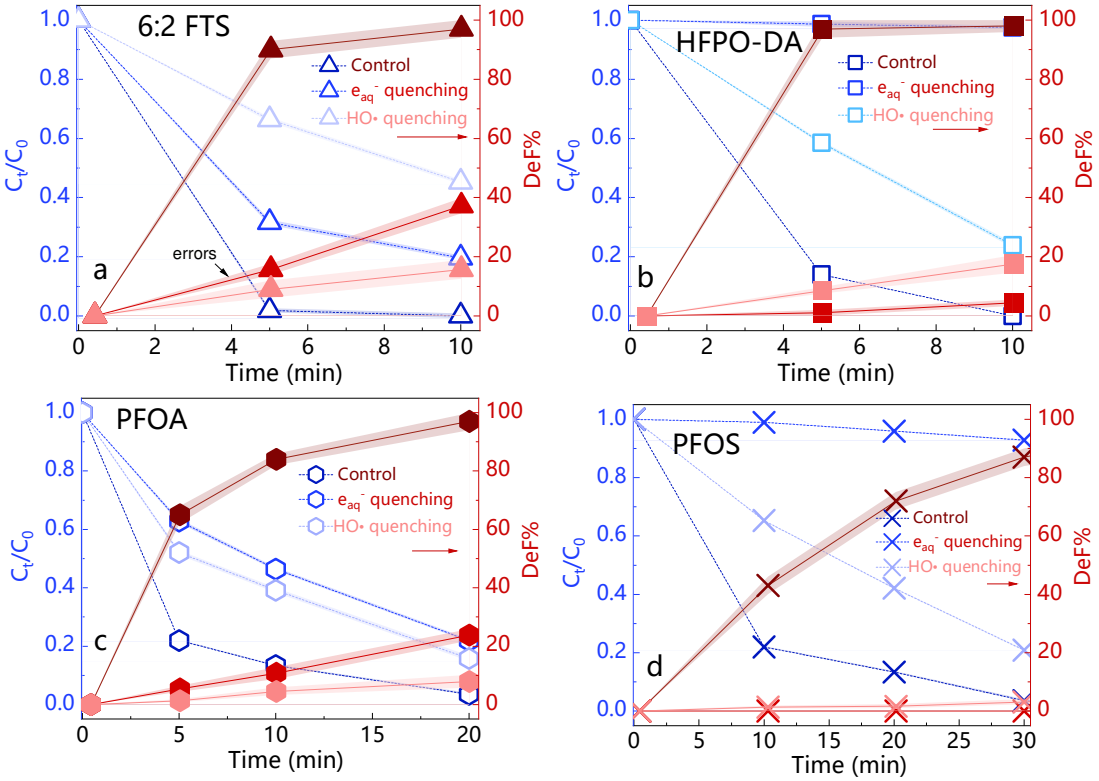
Figure 1 | Spatial reaction regimes, thermodynamic constraints, and Marcus-theory-based kinetic landscapes governing VUV-induced PFAS defluorination. a, d Spatial bifurcation of VUV reaction zones and the corresponding fluorine mass balance. Time-dependent transformation profiles of organic fluorine under VUV irradiation were partitioned into **a** the near-surface zone (direct-photoionization-dominant regime) and **d** the bulk solution (radical-mediated redox regime). The mass fractions $M_{DeF\%}$, M_{F^-}, and $M_{VOF\%}$ represent the molar percentages of structural fluorine mineralization, inorganic fluoride release, and volatile organic fluorine intermediates, respectively, calibrated against the total initial dissolved fluorine mass (C_t/C_0). **b** Correlation between the direct photolytic defluorination rate constant ($\ln k_F$) and the lowest localized C–C/C–F bond dissociation energy (BDE) of the target PFAS molecules. Quantum chemical calculations were performed using DFT at the B3LYP-D3(BJ)/6-311+G(2d,2p) level

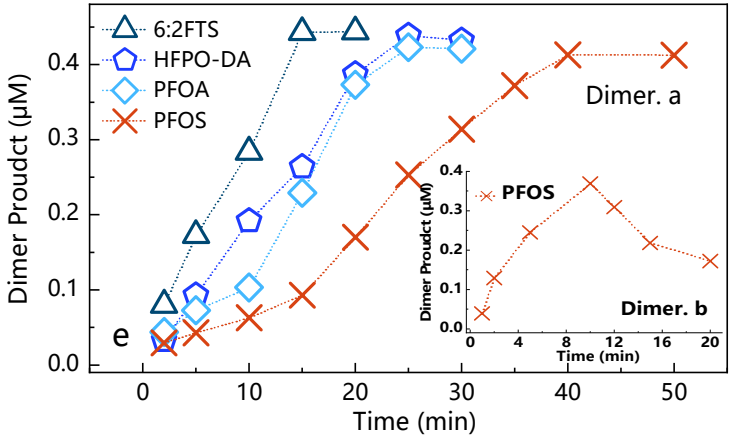
of theory, together with the SMD polarizable continuum model, to systematically evaluate the localized C–F and C–C BDE of all target PFAS structures in the aqueous phase and identify the minimum BDE value[16]. **c** Microscopic model of VUV-induced direct photocleavage. The schematic illustrates nonselective and continuous bond cleavage when the photon energy exceeds the corresponding bond-energy threshold. **e** Defluorination-degradation kinetic plots for distinct PFAS structural classes. The multistructure kinetic matrix correlates the specific defluorination rate constant ($\ln k_F$, representing the rate of total fluorine release) with the parent compound degradation rate constant ($\ln k_G$), representing the rate of decay of the initial molecular structure). The dashed diagonal line indicates the theoretical baseline where $k_F = k_G$. **f** Quantum chemical free-energy profiles based on Marcus theory. Calculated thermodynamic-kinetic landscapes for sequential mineralization steps. The fundamental parameters governing electron-transfer kinetics were computed using the standard Marcus expression[17]: $\Delta G^{\ddagger} = \frac{(\Delta G+\lambda)^2}{4\lambda}$, where $\Delta G^{\ddagger}$ represents the activation free-energy barrier derived from the transition-state threshold, ΔG represents the net thermodynamic driving force calculated as the standard Gibbs free-energy change between the reactant and product states, and λ represents the total reorganization energy required to realign the nuclear coordinates (λ_{in}) and solvent degrees of freedom (λ_{out}) before electron transfer[9, 18].

Transient Dimeric Intermediates Unveiling Kinetic Degradation Barriers

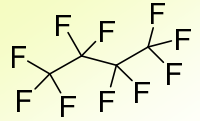
To distinguish the contributions of reductive and oxidative pathways in the coexisting e_{aq}^- and HO• VUV system, selective radical scavenging experiments were conducted (Fig. 2a-d). Quenching of e_{aq}^- isolated the reductive hydrodefluorination pathway, which governs the initial cleavage and defluorination kinetics of HFPO-DA and PFOS. In contrast, for 6:2 FTS and PFOA, suppression of e_{aq}^- had limited impact on initial degradation but significantly hindered deep defluorination. Across all representative PFAS compounds, the decrease in DeF% upon HO• removal exceeded the corresponding decrease in DeG%, indicating that while e_{aq}^- initiates activation, HO• plays a decisive role in downstream transformation. Under HO•-quenched conditions, time-resolved high-resolution TOF-MS analysis enabled the detection of transient intermediates, revealing two distinct dimeric species (Fig. 2 f, and Supplementary Figure 3). *Dimer a* (m/z 218.98) was consistently observed across all systems, exhibiting a continuous increase in concentration during the reaction. Dimer b (m/z 352.92) was uniquely detected in PFOS systems, displaying a transient accumulation followed by rapid decay. The highly hydrophilic structure of *Dimer b*, characterized by abundant –OH and $–SO_3^-$ groups[19, 20], reduces ionization efficiency and chromatographic retention, thereby creating a substantial analytical limitation. This explains why such cross-linked intermediates, analogous to perfluorodicarboxylate dimers, are often overlooked in conventional mass spectrometric analyses[10].

Integration of non-targeted HRMS data with DFT-derived activation barriers enabled the construction of a comprehensive mineralization pathway network (Figure 1g). PFAS degradation involves a complex interplay between e_{aq}^- and HO•$^-$ mediated pathways, with kinetic barriers ($\Delta G^{\ddagger}$) ranging from <10 to 32 kcal/mol[9, 21]. Although reductive defluorination promotes initial chain shortening, critical reaction bottlenecks remain. Specifically, the resulting C_2 radical intermediates follow divergent pathways; they undergo unhindered dimerization ($\Delta G^{\ddagger}$=0 kcal/mol) to form stable dimers, or partial reduction ($\Delta G^{\ddagger}$= 1.8 kcal/mol) to yield VOFs, both of which severely restrict complete mineralization in purely reductive systems. Notably, when HO• is selectively quenched, HRMS analysis reveals substantial accumulation of two dimeric bypass products, a symmetric perfluorinated carbon-chain dimer (*Dimer a*, m/z 218.99, in the four-PFAS system), and a highly asymmetric, polyhydroxylated assembly (*Dimer b*, m/z 352.92, detected only during PFOS degradation). Through accurate-mass profiling by high-resolution TOF-MS, these dimeric compounds, which have distinct polarity and surface-charge characteristics, can be readily distinguished from adjacent fluorinated matrices. Specifically, the rigid perfluorinated carbon-chain skeleton of Dimer a results in prolonged retention on hydrophobic stationary phases, whereas the polyhydroxylated functional topology of Dimer b induces strong polar interactions, producing a markedly earlier column retention time[7]. Intriguingly, the oxidative interception pathway overcomes these energetic traps by rapidly blocking the formation of C_2 dimers and volatile organic fluorides through a nearly barrierless ketonization process ($\Delta G^{\ddagger}\approx 0$ kcal mol^{-1}). Subsequently, the unstable intermediates undergo further reduction to produce charged trifluoroacetate (TFA, $\Delta G^{\ddagger}$= 11–13.5 kcal mol^{-1}), which interacts with H^+ ions generated in the system from liberated hydrofluoric and carbonic acids[22], allowing complete decomposition into short-chain carboxylates and acetate. This competitive redox coupling redirects the reaction coordinate toward complete defluorination.



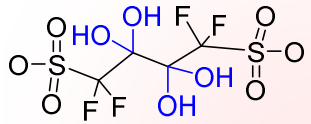


f



Dimer. a: *m/z* 218.98

C–F bond:
114.7~125.5kcal/mol



Dimer. b: *m/z* 352.92

Abundant strongly hydrophilic functional groups

g. Degradation Pathways and Kinetic Energy Barriers of PFASs

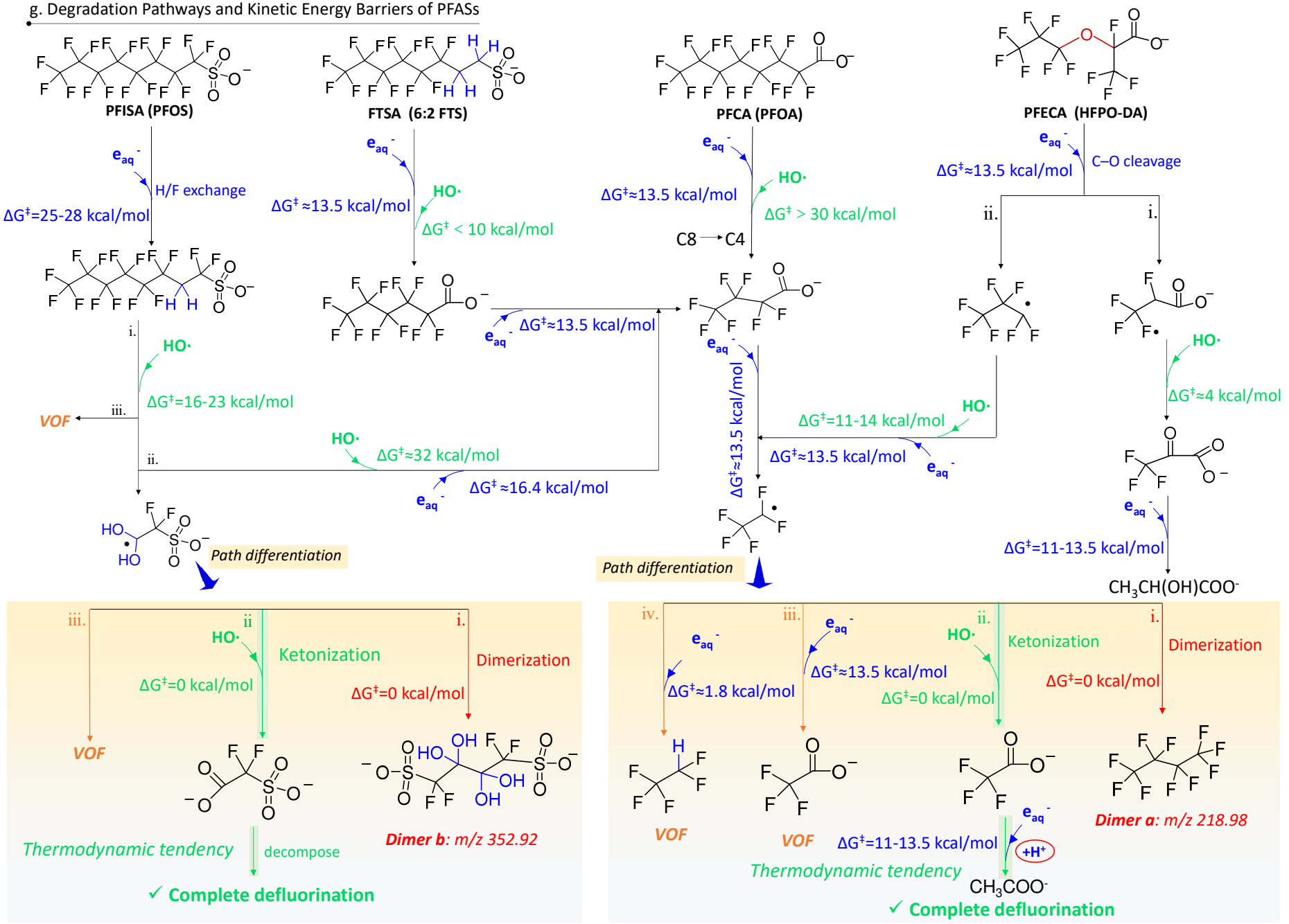


Fig. 2 | Scavenging-induced efficiency variations resolving transient dimeric structures and theoretical mineralization energy trajectories during PFAS degradation. a–d, Experimental configurations for competitive radical tracking and selective pathway isolation during VUV irradiation. Reductive hydrodefluorination mediated by e_aq^- was isolated through complete scavenging of HO• by adding para-chlorobenzoic acid (p-CBA, 5.0 mM stock solution, $k_{HO•+p\text{-}CBA} = 5.0 \times 10^9\ M^{-1}\ s^{-1}$) [23]. Selective identification of oxidative mineralization was achieved through complete interception of e_aq^- by continuous saturation with nitrous oxide (N_2O gas mix, $ke_aq^- + N_2O = 9.1\times10^9\ M^{-1}s^{-1}$) [24]. The reductive mechanism attributed to e_aq^- may include minor contributions from hydrogen radicals (H•), because N_2O also reacts with H• ($k_{H•}+N_2O = 2.1\times10^6\ M^{-1}s^{-1}$) [25]; however, definitive kinetic differentiation between the contributions of e_aq^- and H• was not performed within the scope of this study. **e–f,** Time-dependent concentration profiles of two PFAS intermediates (*Dimer a and b* (inset, detected exclusively in the PFOS degradation system)) across the four target PFAS matrices (**e**) and the corresponding structural configurations (**f**) of cross-linked dimeric intermediates under HO•-scavenging conditions. Detection of Dimer b requires immediate post-sampling chemical quenching with a methanol-catalase mixture (50 mM residual concentration), followed by cryogenic immobilization at -80°C. **g,** Divergent transformation pathways and corresponding activation free-energy barriers ($\Delta G^{\neq}$) for competitive reactions between transient PFAS intermediates and radical species (e_aq^- and HO•). The $\Delta G^{\neq}$ values for reductive pathways mediated by e_aq^- were evaluated using Marcus electron-transfer theory, whereas those for oxidative pathways driven by HO• attack were quantified using transition state theory (TST) through DFT simulations. Modeling these progressive pathways requires explicit matching of spin multiplicities for open-shell species and the strategic placement of explicit water molecules around localized carbanion centers to prevent distortion of transition-state energies.

Wavefunction Rationalization of Radical Interception

To clarify the structural origin of efficiency limitations in PFAS hydrodefluorination, the evolution of thermodynamic and kinetic descriptors along the chain-scission sequence was quantified. As shown in the photon economy profile (Figure 3), long-chain precursors exhibit positive adiabatic electron affinities (AEA) and moderate reorganization energies (λ), enabling favorable e_{aq}^- capture[18]. However, progressive chain truncation to ultra-short C2 intermediates, such as $\cdot CF_2CF_3$ and $\cdot OH_2CF_2SO_3^-$ (Figure 2g), results in a sharp decline in both AEA and vertical electron affinity (VEA), leading to negative values. This thermodynamic limitation, combined with increased coulombic repulsion, renders electron injection unfavorable ($\Delta G_{red}>0$)[26, 27], thereby halting reductive defluorination. Under reductive conditions, these intermediates are redirected into barrierless recombination pathways, forming closed-shell dimers (*Dimer a*: C_4F_{10}; *Dimer b*: $-O_3SCF_2C(OH)_2C(OH)_2CF_2SO_3^-$). These products resist further transformation through distinct mechanisms: *Dimer a* remains chemically inert due to its stable perfluorocarbon framework, whereas *Dimer b* is stabilized within a hydrated matrix that inhibits reactive interception. Alternatively, hydrogen abstraction in proton-rich environments yields volatile fluorinated compounds such as CH_3CF_3[7, 22], posing atmospheric risks. The VUV-driven synergistic system overcomes this limitation through asymmetric oxidative interception. DFT-based wavefunction analysis shows that C2 radicals possess highly localized Hirshfeld spin densities (ρ=91.2% and 93.4%) and elevated electrophilic Fukui indices (f^-=0.4562 and 0.4218) at carbon centers. This electronic configuration promotes selective electrophilic attack by HO•, enabling near barrierless radical coupling ($\Delta G_{oxidation}^{\ddagger}\approx 0$). Because this pathway is more thermodynamically favorable than dimerization ($\Delta G_{oxidation} \ll \Delta G_{dimerization}$)[10], recombination is effectively suppressed. The resulting oxidative transformation converts transient radicals into unstable fluorinated alcohol intermediates, which undergo spontaneous intramolecular ketonization followed by nucleophilic attack ($f^+>0$) by H_2O. This sequence drives the continuous release of inorganic species, ultimately yielding CO^2, F^-, and SO_4^{2-} without accumulation of volatile byproducts.

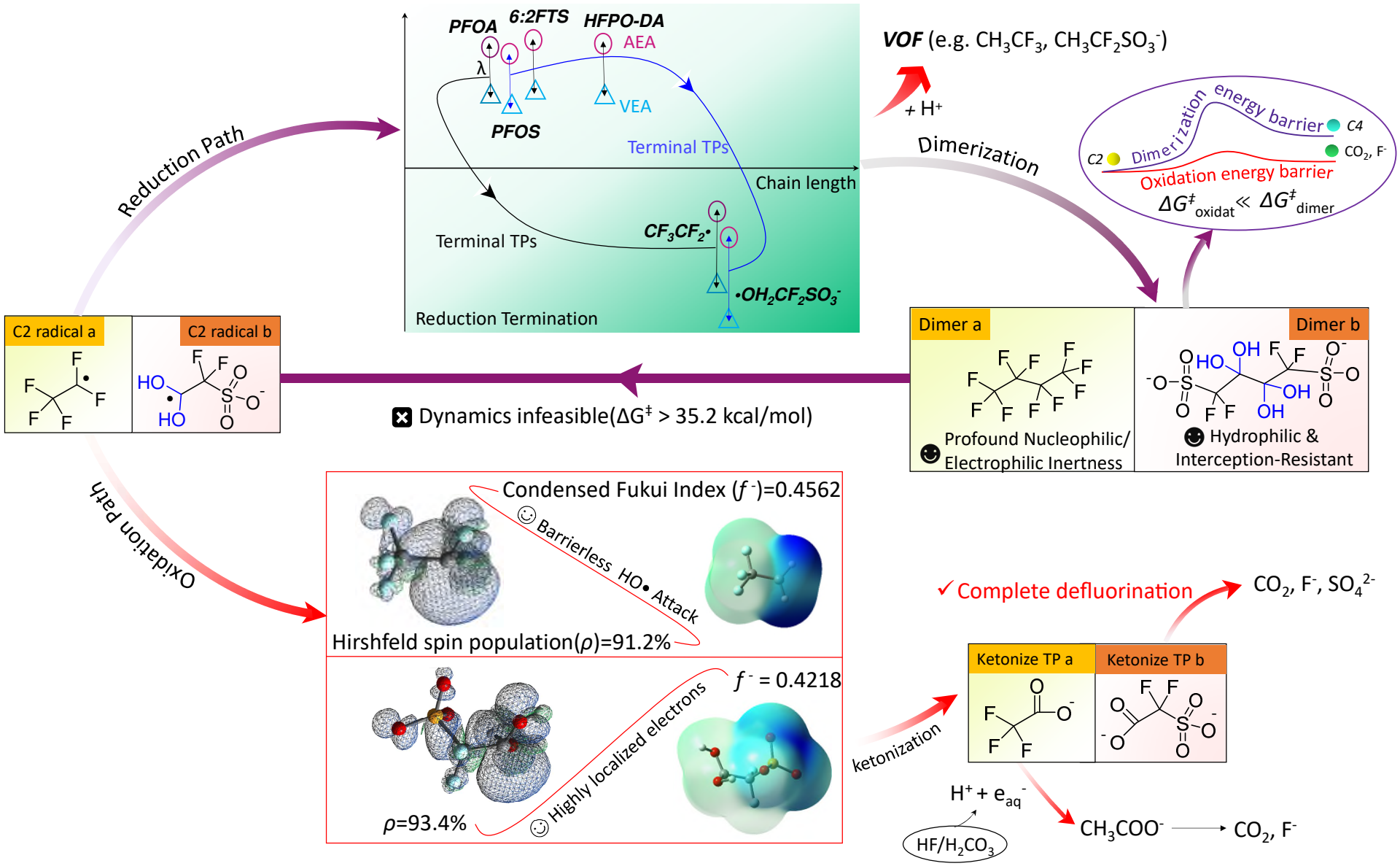


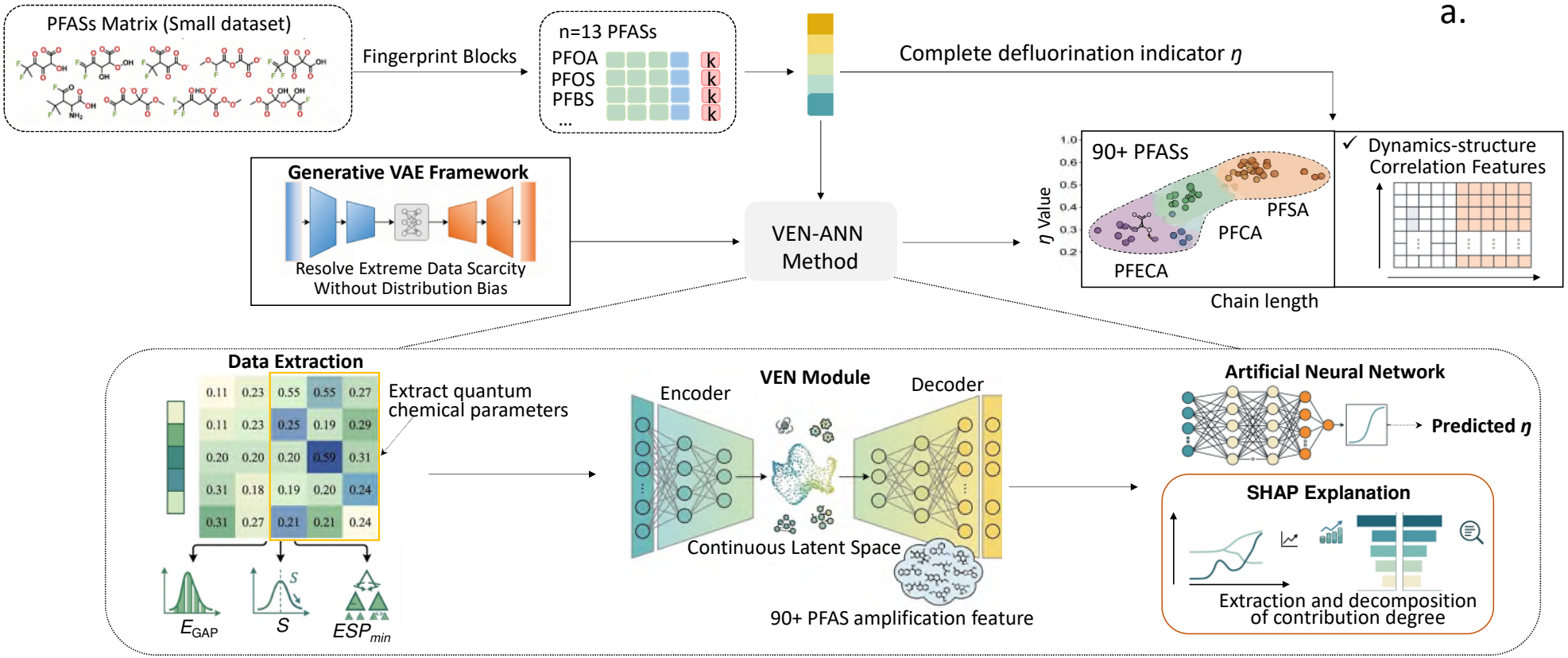
Fig. 3 | Quantum chemical and thermodynamic mechanisms of oxidative interception preventing radical dimerization during PFAS degradation in the VUV system. Energy profiles and reaction coordinates of representative PFAS (PFOA, PFOS, HFPO-DA, and 6:2 FTS) along the reduction pathway, including vertical electron attachment (VEA), adiabatic electron attachment (AEA), and reorganization energy (λ). Chemical structures of representative intermediate radicals (C_2 radical a and b) and their corresponding dimerization products (Dimer a and b). The purple arrow indicates the conventional reduction-termination pathway leading to stable terminal dimerization products. The

blue curve illustrates the thermodynamic bottleneck at which the two-carbon perfluoroalkyl radical cannot undergo further reduction. The red trace depicts the oxidative interception pathway leading to ketonized TPs (Ketonized TP a and b), which subsequently undergo complete defluorination and mineralization into CO_2, F^-, and SO_4^{2-}. The 3D isosurfaces show the Hirshfeld spin population (ρ) and condensed Fukui index (f^-), identifying the specific reactive sites that govern barrierless HO• attack and spontaneous oxidation ($\Delta G_{oxidation} \approx 0$).

Data-Augmented Machine Learning Mapping the Oxidative/Reductive Synergy Index ($\eta_{G/F}$)

To resolve the macro-kinetic dependencies governing concurrent advanced oxidation and reduction processes (AO/RPs) within the VUV photochemical system, a generative Variational Autoencoder (VAE) framework was employed to expand the experimental 13-PFAS dataset into a high-density library containing over 90 congeners (Figure 4a). As shown in the predictive performance matrix (Supplementary Table 2), conventional baseline models exhibited limited predictive capability ($R^2 < 0.50$), failing to capture the non-linear, multi-radical degradation behavior. In contrast, the optimized VAE-Artificial Neural Network (VAE-ANN) model achieved robust generalization, with a test-set R^2 of 0.801—0.876 and reduced root-mean-square error (Figure 4b). Additional validation analyses, including kernel density estimations and cross-model validation heatmaps (Supplementary Figure 4–5), confirm that reconstruction of continuous latent-space topology effectively addresses data scarcity without introducing distributional distortion[28, 29].

To quantitatively balance the multi-radical interaction network, a stoichiometric synergy parameter, $\eta_{G/F,}$ was defined to represent the optimal stoichiometric ratio of coexisting oxidants to reductants required for complete, non-toxic defluorination High-throughput VAE-ANN screening evaluated this index across structurally diverse compounds, ranking the top 20 PFAS candidates with the highest $\eta_{G/F}$ requirements (Figure 4c). The screening results of the top 20 PFAS candidates exhibit excellent alignment with both the experimental radical-quenching profiles (Figure 2a-d) and the extrapolated degradation pathways of the four representative PFASs. PFSAs consistently anchor the highest $\eta_{G/F}$ echelons, headlined by short-chain homologues (e.g., PFPeS and PFBS) whose peak metrics approach 8.0–10.0, closely followed by FTSAs (such as 4:2 and 6:2 FTS). Cause short-chain architectures necessitate an intensified oxidative flux to navigate the reductive kinetic bottlenecks encountered during their convergence toward short-chain (C4-C5) carboxylate intermediates[8, 30]. Conversely, PFCAs partition into a much lower, more moderate $\eta_{G/F}$ regime (0.35–0.45), scaling inversely from PFBA down to long-chain configurations like PFTrDA. This systematic downward trend derive from the expanded perfluorinated framework of long-chain homologues offers a higher density of electrophilic sites[21, 31]. To uncover the intrinsic mechanisms driving these macroscopic variations, SHAPley Additive exPlanations (SHAP) were employed to interpret the VAE-ANN model descriptors (Figure 4d), corroborating the rankings observed in Figure 4c. Quantum chemical parameters, specifically the HOMO–LUMO gap (E_{GAP}) and molecular softness (S), exert the most profound impact, accounting for over 65% of the feature contribution. The high $\eta_{G/F}$ values of short-chain PFSAs and FTSAs are driven by their high E_{GAP} and localized charge distributions, which restrict initial single-electron reduction and demand a heavy oxidative commitment. However, as the perfluorinated carbon chain length (n_C) extends from C4 to C8 and beyond, a critical molecular softness threshold ($S > 0.14$) is surpassed. In tandem with shifts in surface electrostatic potentials (ESP_{min} and $ESP_{pos\ per}$), this increased softness enhances inductive effects and local susceptibility to reductive cleavage. Consequently, the reliance on a dominant oxidative flux diminishes for longer chains, causing the required $\eta_{G/F}$ to decrease asymptotically. This molecular evolution explains why early-stage degradation transitions toward rigorous oxidative control only as chain shortening yields the highly resilient, terminal C2 intermediates.


a.
PFASs Matrix (Small dataset)
Fingerprint Blocks
n=13 PFASs
PFOA
PFOS
PFBS
...
k
Complete defluorination indicator η
Generative VAE Framework
Resolve Extreme Data Scarcity
Without Distribution Bias
VEN-ANN
Method
90+ PFASs
PFSA
PFCA
PFECA
η Value
Chain length
✓ Dynamics-structure
Correlation Features
Data Extraction
Extract quantum
chemical parameters
E_GAP
S
ESP_min
VEN Module
Encoder
Decoder
Continuous Latent Space
90+ PFAS amplification feature
Artificial Neural Network
Predicted η
SHAP Explanation
Extraction and decomposition
of contribution degree

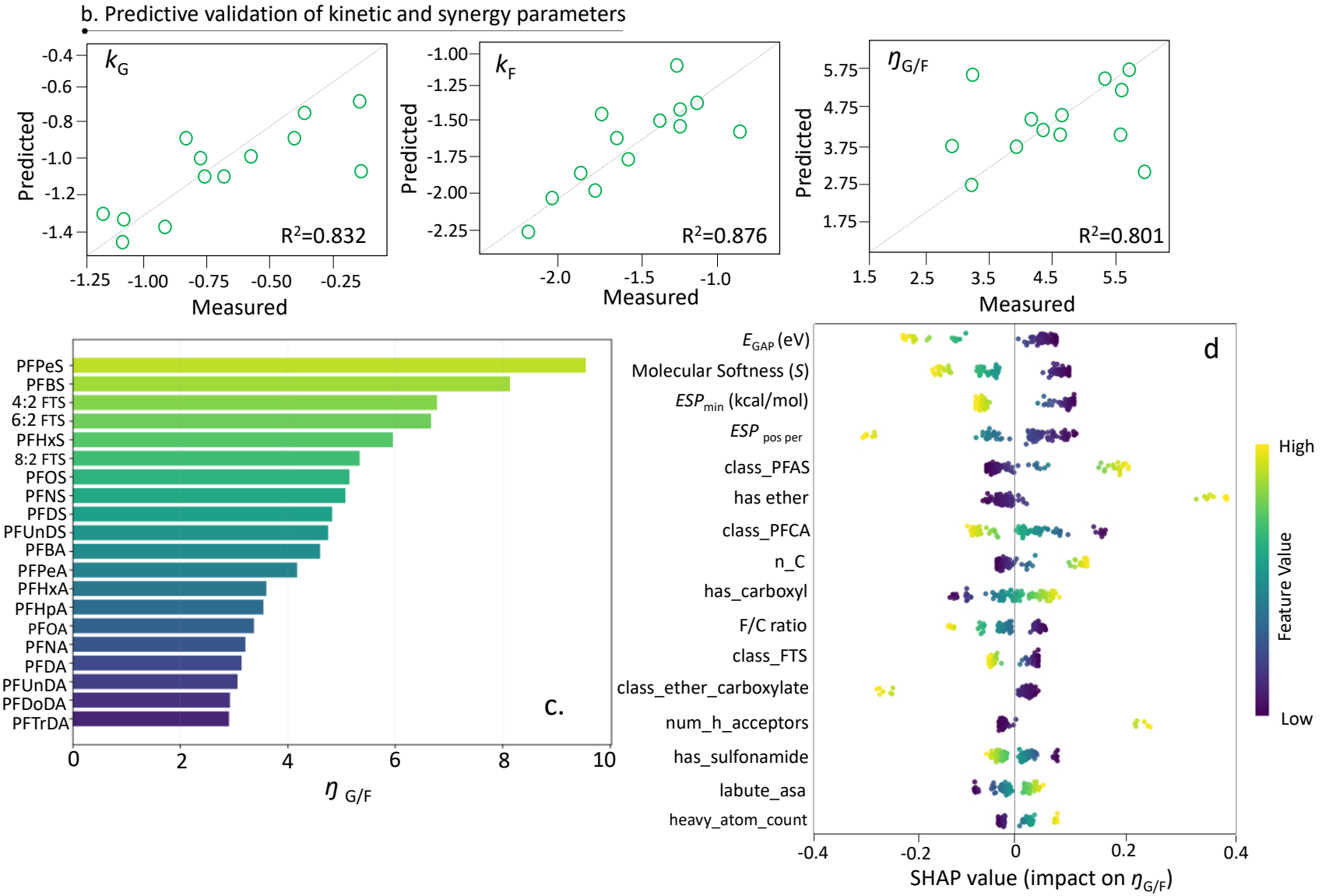


Fig. 4 | Variational Autoencoder (VAE)-enhanced kinetic prediction and structural synergy tracking of PFAS degradation. a. Schematic workflow of unsupervised data augmentation using a generative VAE framework combined with downstream predictive neural networks. **b.** Predictive validation of kinetic and stoichiometric synergy parameters. Parity plots comparing experimental (measured) values with predictions from the generative VAE-ANN model for the pseudo-first-order oxidative rate constant (k_G), reductive rate constant (k_F), and oxidant/reductant ratio ($\eta_{G/F}$) required for complete fluorine removal. The diagonal solid grey lines indicate the ideal 1:1 relationship

(perfect prediction), with green open circles representing individual validation data points. **c.** High-throughput VAE-ANN screening profiles mapping the top 20 PFAS candidates ranked according to the $\eta_{G/F}$ value. **d.** SHapley Additive exPlanations (SHAP) beeswarm visualization. Global feature-importance and contribution mapping of the 16 primary molecular and quantum chemical descriptors controlling the predicted $\eta_{G/F}$ index. The *x*-axis shows the SHAP value, which defines the directional effect of each feature on the VAE-ANN model output.

Conclusion and Outlook

The customized AO/RP system demonstrates that purely reductive conditions encounter an energetic limitation at the C2 intermediate stage, resulting in pathway stagnation due to the formation of stable dimeric species or volatile organic byproducts. The introduction of synchronized asymmetric oxidative radical coupling effectively removes this limitation. Localized orbital polarization of short-chain radicals promotes near barrierless electrophilic attack by HO•. This mechanism circumvents the limitation imposed by reduced electron affinity, enabling subsequent nucleophilic attack by H_2O, spontaneous ketonization, and complete conversion into inorganic end products without accumulation of toxic intermediates. This strategic pathway undoubtedly unlocks a viable solution to the persistent kinetic bottleneck of PFAS degradation—namely, dead-end accumulation of trifluoroacetic acid (TFA)[32] and resilient short-chain carboxylic intermediates. Nevertheless, when confronted with the vast expanse of tens of thousands of emerging PFAS alternatives harboring diverse functional groups[33], achieving absolute defluorination necessitates a synergistic paradigm shift at the intersection of environmental engineering and de novo molecular design. The evolution of the $\eta_{G/F}$ index indicates that treatment systems should dynamically shift from reductive conditions suitable for long-chain cleavage toward oxidative regimes as degradation proceeds. Reactor configurations incorporating staged or compartmentalized dosing of oxidants and reductants may enable maintenance of optimal local stoichiometry throughout the process. The predictive performance of the VAE-ANN framework further substantiates the value of data-augmented modeling in overcoming experimental limitations. These approaches establish a robust platform for prospective molecular design, highlighting that mitigating the environmental risks of PFAS should extend beyond a narrow focus on carbon chain length and head-group electrophilicity. Instead, emphasis must shift toward aligning intrinsic molecular features, such as the molecular softness threshold, with the reaction synergy index, thereby creating the internal structural traits and external operational conditions necessary to achieve complete mineralization of PFAS.

Methods

VUV Irradiation and PFAS Compounds Analytical Procedures

Photochemical degradation experiments were conducted using a continuous-flow VUV irradiation system. The reactor consisted of a stainless steel chamber equipped with a centrally aligned VUV light source (254/185 nm, transmittance of VUV = 95%), with solution flow maintained at a constant rate by a peristaltic pump. The experimental configuration is illustrated in Supplementary Figure 6. Target PFAS compounds and volatile intermediates were quantified using high-performance liquid chromatography coupled with tandem mass spectrometry (HPLC-MS/MS, API 3200; Applied Biosystems). Short-chain carboxylic products, including lactic and acetic acids, were monitored using LC-MS. Fluoride ions (F^-) were quantified by ion chromatography (Dionex ICS-2000; Thermo Fisher Scientific) using an eluent generator with 20 mM KOH at a flow rate of 1.0 mL min^{-1}. Total organic fluorine (OF) was determined by combustion ion chromatography (CIC, HIC-20A SUPER; Shimadzu), in which samples were mineralized at 950 °C under oxygen, followed by dilution through solid-phase microcolumns. Non-targeted analysis of transient intermediates was performed using high-resolution time-of-flight mass spectrometry (Q-TOF-MS; Sciex). All samples were filtered and neutralized prior to analysis to minimize instrumental interference and maintain stable chromatographic conditions.

Theoretical Calculations and Density Functional Theory (DFT)

All molecular structures and electronic properties were calculated using density functional theory (DFT) as implemented in Gaussian 16. Geometry optimizations and frequency calculations were performed

using the B3LYP functional with Grimme dispersion correction [B3LYP-D3(BJ)] and the 6–311+G(2d,2p) basis set[16]. Transition states and radical species were verified through intrinsic reaction coordinate (IRC) analysis and frequency calculations to ensure correct characterization. Spin density distributions and Mulliken charges were analyzed using the Multiwfn package to characterize electronic localization and polarization.

Reduction-related thermodynamic parameters were evaluated using vertical electron affinity (VEA) and adiabatic electron affinity (AEA). The VEA was calculated as the energy difference between neutral and anionic states at the optimized neutral geometry: VEA=$E_{\text{neutral}} - E_{\text{anion(at neutral geometry)}}$[18]. The AEA was determined from the energy difference between fully optimized neutral and anionic structures, including zero-point energy (ZPE) corrections: AEA= (E_{neutral} +$\text{ZPE}_{\text{neutral}}$)−($E_{\text{anion}}$+ ZPE $_{\text{anion}}$)[8, 17].

Data Augmentation via Variational Autoencoder

The original experimental dataset was expanded into a high-density virtual library of over 90 PFAS congeners (Supplementary Text 3) using a deep generative VAE framework. The VAE architecture consisted of a probabilistic encoder containing two hidden layers (128 and 64 neurons, respectively) with ReLU activation functions, which mapped the input features into a compact, two-dimensional continuous latent space. A symmetric probabilistic decoder reconstructed the synthetic data using a linear activation function. The statistical consistency of the VAE-generated synthetic database was validated via Kernel Density Estimation (KDE) to prevent distributional distortion. Using 18 optimal quantum chemical and electrostatic descriptors identified through Lasso regression, we systematically trained and compared six supervised ML regressors (Elastic Net, SVM, Random Forest, XGBoost, RNN, and ANN)[29, 34, 35]. The dataset was randomly split into training (80%) and test (20%) subsets, with hyperparameter tuning performed via grid search and five-fold cross-validation. To compare the prediction accuracy of these models in predicting k_G, k_F and $\eta_{G/F}$, the coefficient of determination(R^2) and Root Mean Square Error (RMSE) were calculated using eqs 1 and 2, respectively[28, 29, 36]. The optimized VAE-ANN model achieved robust generalization with a test-set R^2 of 0.80-0.87. To overcome the "black box" nature of neural networks, SHAPley Additive exPlanations (SHAP) and Partial Dependence Plots (PDPs) were integrated to resolve the highly non-linear molecular mechanisms governing $\eta_{G/F}$.

$$R^2 = 1 - \frac{\sum_{i=1}^{N}(y_p^i - y_t^i)^2}{\sum_{i=1}^{N}(y_t^i - y_m^i)^2} \qquad (1)$$

$$RMSE = \sqrt{\frac{\sum_{i=1}^{N}(y_t^i - y_p^i)^2}{2a}} \qquad (2)$$

where y_p^i and y_t^iwere the predicted and true values of the output, respectively, y_m was the mean value of all output values, and N was the number of data samples.

Acknowledgments

We thank the funding support from the National Natural Science Foundation of China (Grant No. 52470009); Beijing Municipal Science and Technology Plan: International (Hong Kong, Macao, and Taiwan) Joint Research and Development Project (Grant No. Z251100007125027）

References

1. *Evich, M.G. et al. Per- and polyfluoroalkyl substances in the environment. Science **375** (2022).*
2. *Shira Joudan, R.J.L. Taking the "F" out of forever chemicals. Science **377** (2022).*
3. *Cui, J., Gao, P. & Deng, Y. Destruction of Per- and Polyfluoroalkyl Substances (PFAS) with Advanced Reduction Processes (ARPs): A Critical Review. Environmental Science & Technology **54**, 3752-3766 (2020).*

4. *Liu, Z. et al. Near-Quantitative Defluorination of Perfluorinated and Fluorotelomer Carboxylates and Sulfonates with Integrated Oxidation and Reduction. Environmental Science & Technology **55**, 7052-7062 (2021).*
5. *Mirzaei, M., Asgarpour Khansary, M. & Mohseni, M. Degradation of PFOS in concentrated saline waste streams using UV/ Sulfite process: Critical impact of aggregation. Journal of Hazardous Materials **496** (2025).*
6. *Wang, X. et al. Alcohols radicals can efficiently reduce recalcitrant perfluorooctanoic acid. Water Research **245** (2023).*
7. *Kim, J. et al. Kinetics and proposed mechanisms of hexafluoropropylene oxide dimer acid (GenX) degradation via vacuum-UV (VUV) photolysis and VUV/sulfite processes. Journal of Hazardous Materials **463** (2024).*
8. *Zhang, Y., Liu, J., Ghoshal, S. & Moores, A. Density Functional Theory Calculations Decipher Complex Reaction Pathways of 6:2 Fluorotelomer Sulfonate to Perfluoroalkyl Carboxylates Initiated by Hydroxyl Radical. Environmental Science & Technology **55**, 16655-16664 (2021).*
9. *Tan, S. et al. Unravelling the structure-dependent defluorination mechanisms of per- and polyfluoroalkyl substances by hydrated electrons in UV/sulfite. Nature Water **3**, 734-745 (2025).*
10. *Gao, J. et al. Photochemical degradation pathways and near-complete defluorination of chlorinated polyfluoroalkyl substances. Nature Water **1**, 381-390 (2023).*
11. *Banayan Esfahani, E., Asadi Zeidabadi, F., Jafarikojour, M. & Mohseni, M. Photo-oxidative/reductive decomposition of perfluorooctanoic acid (PFOA) and its common alternatives: Mechanism and kinetic modeling. Journal of Water Process Engineering **61** (2024).*
12. *Guan, Y. et al. Near-complete destruction of PFAS in aqueous film-forming foam by integrated photo-electrochemical processes. Nature Water **2**, 443-452 (2024).*
13. *Gonzalez, M., Oliveros, E., Worner, M. & Braun, A. Vacuum-ultraviolet photolysis of aqueous reaction systems. Journal of Photochemistry and Photobiology C: Photochemistry Reviews **5**, 225-246 (2004).*
14. *Masjoudi, M., Dixit, F., Barbeau, B., Mitch, W. & Mohseni, M. Photodegradation of micropollutants by vacuum-UV (VUV) radiation in potable reuse waters: Promotive and inhibitory effects of free chlorine oxidant. Journal of Environmental Chemical Engineering **13** (2025).*
15. *Calvillo Solís, J.J. et al. Electrochemical Reduction of Perfluorooctanoic Acid (PFOA): An Experimental and Theoretical Approach. Journal of the American Chemical Society **146**, 10687-10698 (2024).*
16. *Ambrosio, F., Miceli, G. & Pasquarello, A. Electronic Levels of Excess Electrons in Liquid Water. The Journal of Physical Chemistry Letters **8**, 2055-2059 (2017).*
17. *Liao, M. et al. Silicate-Confined Hydrogen on Nanoscale Zerovalent Iron for Efficient Defluorination Reactions. Journal of the American Chemical Society **147**, 3402-3411 (2025).*
18. *Biswas, S., Yamijala, S.S.R.K.C. & Wong, B.M. Degradation of Per- and Polyfluoroalkyl Substances with Hydrated Electrons: A New Mechanism from First-Principles Calculations. Environmental Science & Technology **56**, 8167-8175 (2022).*
19. *Marron, E.L., Prasse, C., Buren, J.V. & Sedlak, D.L. Formation and Fate of Carbonyls in Potable Water Reuse Systems. Environmental Science & Technology **54**, 10895-10903 (2020).*
20. *Zhao, B. et al. Direct visible-light-excited flavoproteins for redox-neutral asymmetric radical hydroarylation. Nature Catalysis **6**, 996-1004 (2023).*
21. *Guelfo, J.L. et al. Lithium-ion battery components are at the nexus of sustainable energy and environmental release of per- and polyfluoroalkyl substances. Nature Communications **15** (2024).*
22. *Liu, S. et al. Promotive Effects of Chloride and Sulfate on the Near-Complete Destruction of Perfluorocarboxylates (PFCAs) in Brine via Hydrogen-tuned 185-nm UV Photolysis: Mechanisms and Kinetics. Environmental Science & Technology **58**, 10347-10356 (2024).*

23. *Imoberdorf, G. & Mohseni, M. Modeling and experimental evaluation of vacuum-UV photoreactors for water treatment. Chemical Engineering Science **66**, 1159-1167 (2011).*
24. *Liu, G., Feng, C. & Shao, P. Degradation of Perfluorooctanoic Acid with Hydrated Electron by a Heterogeneous Catalytic System. Environmental Science & Technology **56**, 6223-6231 (2021).*
25. *Xue, Y., Sun, W., Shi, W., Huang, C.-H. & Santoro, D. Prehydrated Electrons Activated by Continuous Electron Transfer Stemmed from Peracetic Acid Homolysis Mediated by Diamond Surface Defects for Enhanced PFOA Destruction. Environmental Science & Technology **58**, 11152-11161 (2024).*
26. *Sarkar, B. et al. Lithium metal-mediated electrochemical reduction of per- and poly-fluoroalkyl substances. Nature Chemistry **18**, 509-518 (2026).*
27. *Bentel, M.J. et al. Enhanced Degradation of Perfluorocarboxylic Acids (PFCAs) by UV/Sulfite Treatment: Reaction Mechanisms and System Efficiencies at pH 12. Environmental Science & Technology Letters **7**, 351-357 (2020).*
28. *Song, T. et al. A Multiagent-Driven Robotic AI Chemist Enabling Autonomous Chemical Research On Demand. Journal of the American Chemical Society **147**, 12534-12545 (2025).*
29. *Wu, J., Ding, Y., Zhu, C., Sui, Q. & Zhou, L. Data-augmented machine learning improves water treatment design: Precise prediction of PPCPs reaction with reactive radicals. Water Research **291** (2026).*
30. *Bentel, M.J. et al. Defluorination of Per- and Polyfluoroalkyl Substances (PFASs) with Hydrated Electrons: Structural Dependence and Implications to PFAS Remediation and Management. Environmental Science & Technology **53**, 3718-3728 (2019).*
31. *Qi, Y. et al. Unveiling the Contribution of Hydrogen Radicals to Per- and Polyfluoroalkyl Substances (PFASs) Defluorination: Applicability and Degradation Mechanisms. Environmental Science & Technology **59**, 1875-1886 (2025).*
32. *Wang, Y. et al. Trifluoroacetic Acid (TFA) Deposition and Accumulation Potential from Future Emissions of HFO-1234yf in China. Environmental Science & Technology **60**, 16830-16840 (2026).*
33. *Pan, Y. et al. Worldwide Distribution of Novel Perfluoroether Carboxylic and Sulfonic Acids in Surface Water. Environmental Science & Technology **52**, 7621-7629 (2018).*
34. *Liang, J. et al. Combination of Density Functional Theory and Machine Learning Provides Deeper Insight of the Underlying Mechanism in the Ultraviolet/Persulfate System. Environmental Science & Technology **59**, 6891-6899 (2025).*
35. *Yang, C., Wu, C., Xie, W., Xie, D. & Hu, P. General reactive element-based machine learning potentials for heterogeneous catalysis. Nature Catalysis **8**, 891-904 (2025).*
36. *Han, Z. et al. Machine-learning-assisted design of a binary descriptor to decipher electronic and structural effects on sulfur reduction kinetics. Nature Catalysis **6**, 1073-1086 (2023).*

Supplementary Files

This is a list of supplementary files associated with this preprint. Click to download.

- SupplementaryInformation.docx